Formation and electronic properties of InSb nanocrosses

Sébastien R. Plissard[1,2]†*, Ilse van Weperen[2]†, Diana Car[1], Marcel A. Verheijen[1,3], George W. G. Immink[3], Jakob Kammhuber[2], Ludo J. Cornelissen[2], Daniel B. Szombati[2], Attila Geresdi[2], Sergey M. Frolov[2,4], Leo P. Kouwenhoven[2] and Erik P. A. M. Bakkers[1,2]*

Signatures of Majorana fermions have recently been reported from measurements on hybrid superconductor–semiconductor nanowire devices. Majorana fermions are predicted to obey special quantum statistics, known as non-Abelian statistics. To probe this requires an exchange operation, in which two Majorana fermions are moved around one another, which requires at least a simple network of nanowires. Here, we report on the synthesis and electrical characterization of crosses of InSb nanowires. The InSb wires grow horizontally on flexible vertical stems, allowing nearby wires to meet and merge. In this way, near-planar single-crystalline nanocrosses are created, which can be measured by four electrical contacts. Our transport measurements show that the favourable properties of the InSb nanowire devices—high carrier mobility and the ability to induce superconductivity—are preserved in the cross devices. Our nanocrosses thus represent a promising system for the exchange of Majorana fermions.

Majorana fermions[1] can arise as pairs of quasi-particles located at the ends of a semiconductor nanowire in contact with a superconductor[2–4]. Interestingly, the quantum properties of Majorana fermions are expected to be protected by topology, becoming insensitive to perturbations, which could make them robust quantum bits[5–7]. Logical operations can be performed by exchanging the positions of two Majorana fermions, that is, by braiding, thereby exploiting their non-Abelian exchange statistics[8]. Following proposals in refs 9 and 10, signatures of Majorana fermions were recently detected in a one-dimensional semiconductor nanowire (with strong spin–orbit interactions) in contact with a superconductor[2–4]. However, currently available single-nanowire devices are not suitable for demonstrating braiding, because Majorana fermions annihilate when they come into close proximity with one another. Recent theories have proposed the use of nanowire junctions to make braiding possible[11–13], by temporarily storing one Majorana fermion in an auxiliary leg of a T-junction while moving the other particle across, or by using a flux-controlled interaction between Majorana fermions in a double T-junction (Supplementary Fig. S1).

Braiding of Majorana fermions imposes three strong requirements on the semiconductor materials. First, to generate Majoranas the material should exhibit strong spin–orbit coupling. Second, the branched wires must form a planar structure to enable electronic device fabrication by standard lithography. Finally, the branched structures should be of high crystalline quality, because for Majorana particles it is important to have nearly ballistic transport, and defects in the wires and at the interface will induce unwanted Majoranas. Despite continuous progress in the control and understanding of nanowire growth[14–16], there are only a few studies that focus on three-dimensional branched nanowire networks[17–23]. Here, we discuss a new approach to growing InSb T- and X-shaped nanostructures from the strong spin–orbit

coupling semiconductor InSb, using a vapour–liquid–solid (VLS) mechanism[24] and gold as the catalyst. We show that all the requirements outlined above are satisfied in our structures.
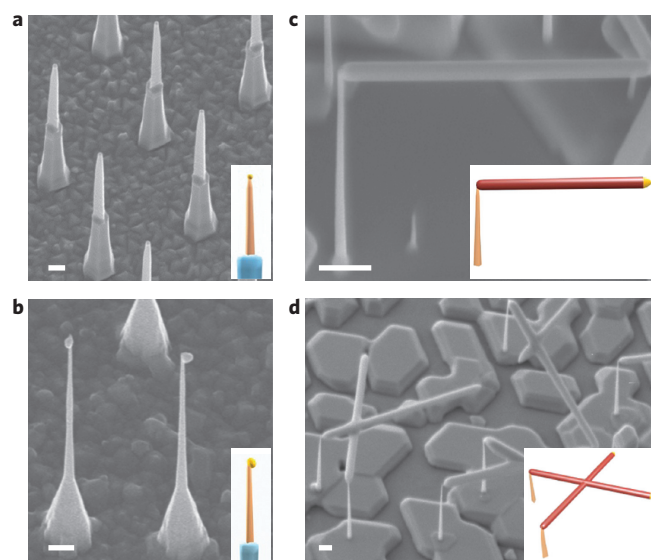
Figure 1 | The four-step process for synthesizing branched InSb nanowires. **a**, A 30° tilted SEM image of the InP/InAs stems. **b**, Au–In droplets on side facets after the annealing step. **c**, InSb nanowire grown parallel to the substrate surface. **d**, InSb nanocrosses resulting from the merging process between two InSb nanowires. All scale bars, 200 nm. Growth times in **a**–**d** are different. Insets: InP, InAs and InSb segments are in blue, orange and red, respectively, and the Au–In droplet is in yellow.

[1]Department of Applied Physics, Eindhoven University of Technology, PO Box 513, 5600 MB Eindhoven, The Netherlands, [2]Kavli Institute of Nanoscience, Delft University of Technology, 2628CJ Delft, The Netherlands, [3]Philips Innovation Services Eindhoven, High Tech Campus 11, 5656AE Eindhoven, The Netherlands, [4]Department of Physics and Astronomy, University of Pittsburgh, 3943 O'Hara Street, Pittsburgh, Pennsylvania 15260, USA, †These authors contributed equally to this work. *e-mail: sebastien.plissard@free.fr; e.p.a.m.bakkers@tue.nl
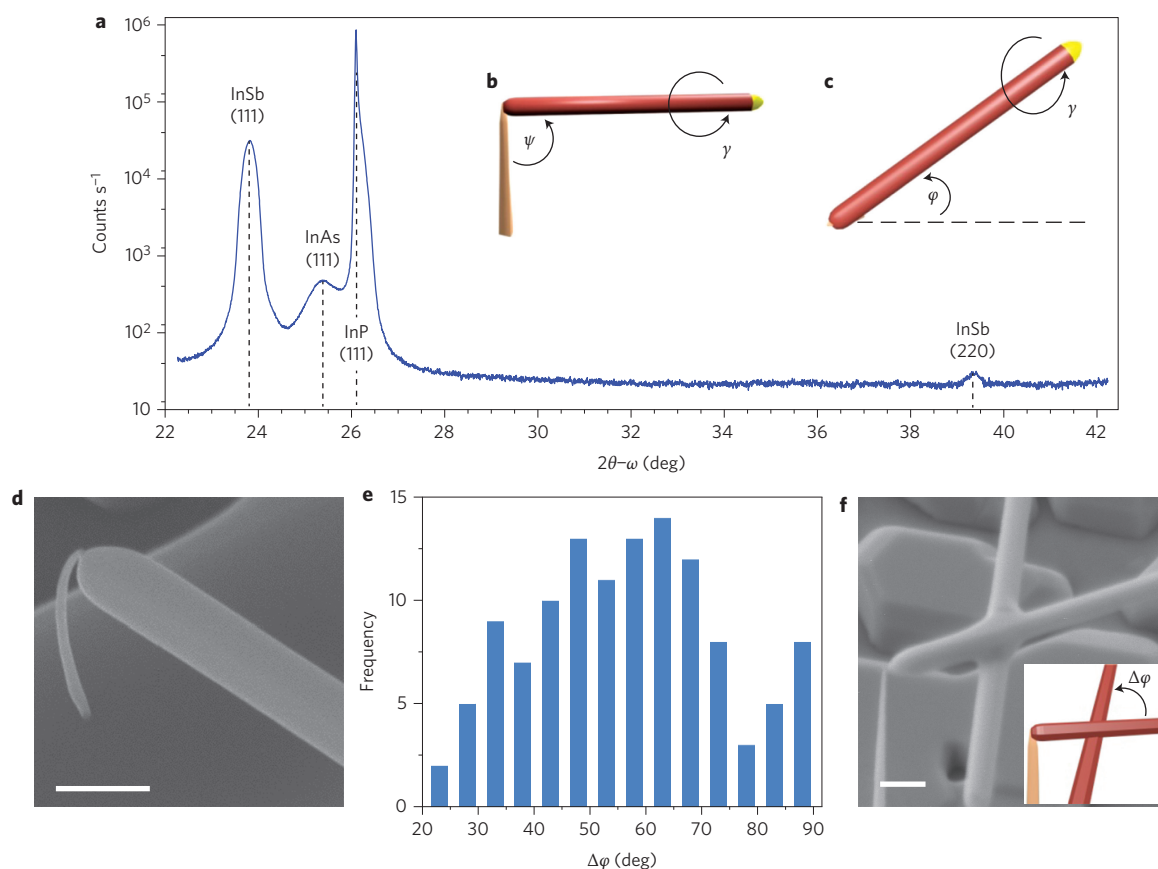
Figure 2 | Merging process for two InSb nanowires. a, Symmetrical (2θ–ω) XRD measurement on an as-grown sample. **b,c**, Side view (**b**) and top view (**c**) schemes of the InSb nanowires grown horizontally. The three angles defining the InSb growth direction are ψ, φ and γ. ψ corresponds to the angle between the vertical stem and the growth direction of the InSb nanowire, φ is the in-plane angle of the InSb nanowire with respect to the $\langle 1\bar{1}0 \rangle$ direction of the InP(111)B substrate, and γ is the rotation angle of the InSb nanowire around its long axis, taking the alignment of the (220) InSb planes with the substrate surface as a reference. **d**, High-resolution SEM image of an InP/InAs stem bent during the merging process. **e**, Statistics about the $\Delta\varphi$ angle between two crossing InSb nanowires. **f**, Example of a branched structure: the two InSb nanowires should have a slight difference in altitude in order to merge into a nanocross. All scale bars, 200 nm.

The crosses grow as single crystals of high mobility, comparable to single InSb nanowires[25].

We start with a qualitative description of the process we developed for the formation of crossed wires. The procedure includes four steps, which are presented schematically in the insets in Fig. 1, accompanied by corresponding scanning electron microscopy (SEM) images. The first step is the fabrication of uniform InP–InAs stems (Fig. 1a) according to the method described in ref. 25. In step 2, the structure is thermally annealed at 470 °C in a reactor chamber without any precursor, resulting in partial evaporation of the InAs nanowire and indium enrichment in the Au–In droplet. Because the particle volume increases and the InAs nanowire diameter decreases, the droplet falls to one of the three {112} InAs side facets (Fig. 1b, Supplementary Fig. S3). It is then possible to start the growth of InSb nanowires in a horizontal direction, parallel to the substrate (Fig. 1c), using the optimal growth conditions (Supplementary Fig. S2) developed in ref. 25 for high-mobility wires[2,26]. If an optimal diameter and density of gold colloids are used, InSb nanowires growing from different stems can meet and merge into nanostructures with T or X shapes (Fig. 1d).

The merging of the wires will now be discussed in more detail. To describe the nanowire intersection, three angles are defined (Fig. 2b,c). ψ corresponds to the angle between the vertical stem and the growth direction of the InSb nanowire, φ is the in-plane angle of the InSb nanowire, and γ is the rotation angle of the

InSb nanowire around its long axis. Interestingly, these different angles are not random, as will be shown below.

SEM side-view inspection of the samples shows that ψ is close to 90°, implying that the tapering of the InAs nanowires is minimal. To investigate the exact crystalline orientation of the InSb wires, X-ray diffraction (XRD) measurements were performed in a symmetric 2θ–ω configuration. Figure 2a shows a diffraction spectrum of the sample, where the (111) peaks of InP, InAs and InSb originate from the stems and a thin layer on the substrate. Importantly, a fourth peak also appears around the InSb(220) Bragg angle (39.3°). The intensity is rather weak due to the small volume of material, but it is still detectable with a standard set-up, and the 2θ full-width at half-maximum is ~0.4°. This peak originates from InSb nanowires having one of their {110} side facets parallel to the substrate surface. The fact that no other sets of InSb lattice planes perpendicular to the $\langle 111 \rangle$ growth direction (for example, (422)) show up in the XRD pattern proves that ψ and γ are fixed to 90° and 0°, respectively (Supplementary Section S2). Because stems and substrate have no horizontal $\langle 111 \rangle$ crystalline directions, this demonstrates that the InSb nanowires have no epitaxial relation with the InP–InAs stems, and the stems only serve as a mechanical support.

To investigate φ, we measured the angle $\Delta\varphi$ between two legs for T- and X-shaped nanostructures (Fig. 2e,f). For this study, more than 100 InSb crosses were transferred onto a SiO$_2$ substrate and imaged from the top to provide a perpendicular
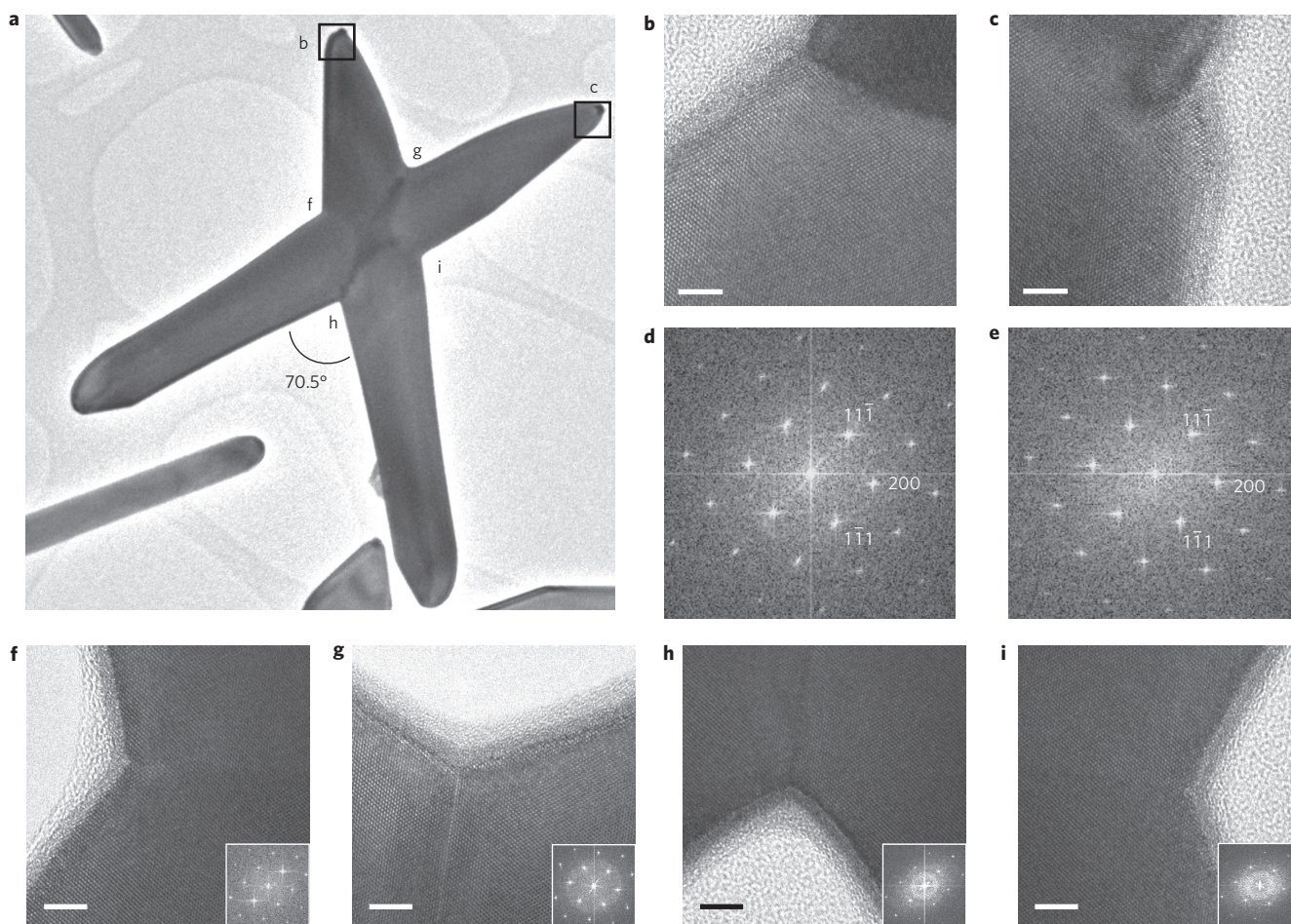
Figure 3 | Crystal structure of a single-crystalline nanocross. a, Low-resolution TEM image of a single-crystalline InSb nanocross. **b,c**, HR-TEM images just below the droplet for both branches. Scale bars, 5 nm. **d,e**, FFT patterns corresponding to **b** and **c**, respectively. The crystalline directions are perfectly superposed, proving the nanocross in **a** is a single crystal. **f–i**, HR-TEM images of each corner of the nanocross and the corresponding FFT pattern showing a single-crystalline orientation. Scale bars, 5 nm.
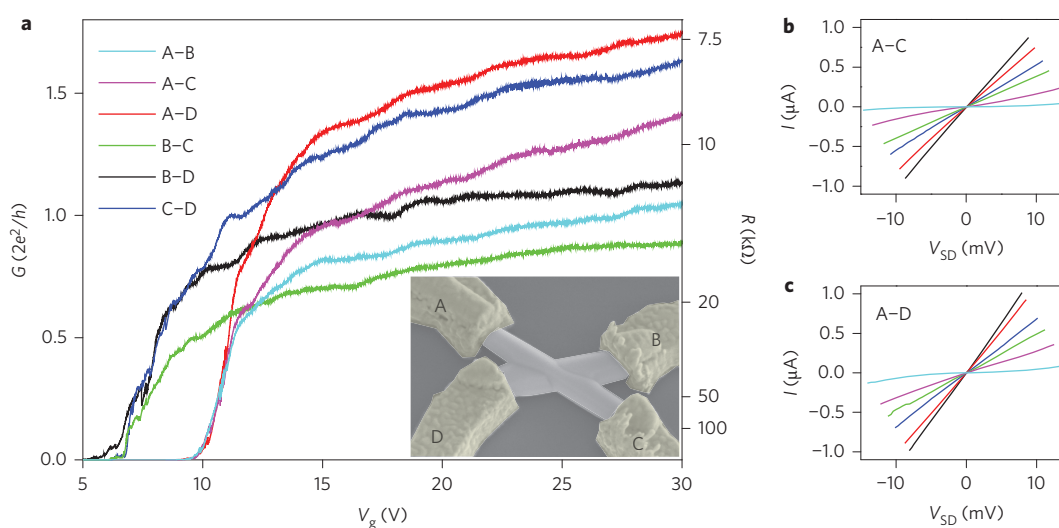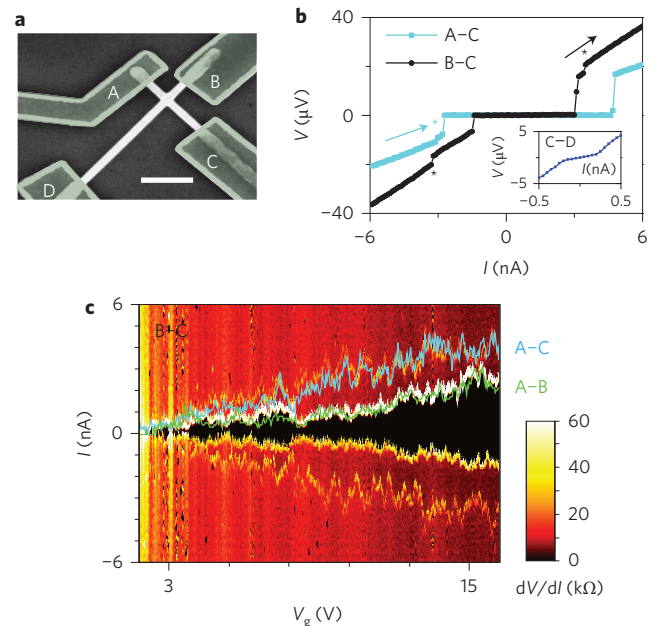

Figure 4 | Transport through a nanocross. All data were taken at a temperature of 4.2 K. **a**, Conductance $G = I/V_{SD}$ of all six contact pairs as a function of gate voltage V_g. V_{SD} is the voltage bias across the device; I is current. For all traces, V_{SD} is between 10 mV (near pinch-off) and 5 mV (at $V_g = 30$ V). Right axis: resistance $R = 1/G$. Inset: SEM image (50° tilted) of the measured nanocross. $\Delta\varphi$, the angle between nanocross legs, is 45°. **b,c**, Bias voltage sweeps of contact pairs A–C (**b**) and A–D (**c**) at several gate voltages V_g. For **b**, from light blue to black, $V_g = 9.8, 10.5, 11.1, 12, 15$ and 22.5 V. For **c**, from light blue to black, $V_g = 9.8, 10.2, 10.7, 11.7, 15$ and 22.5 V.
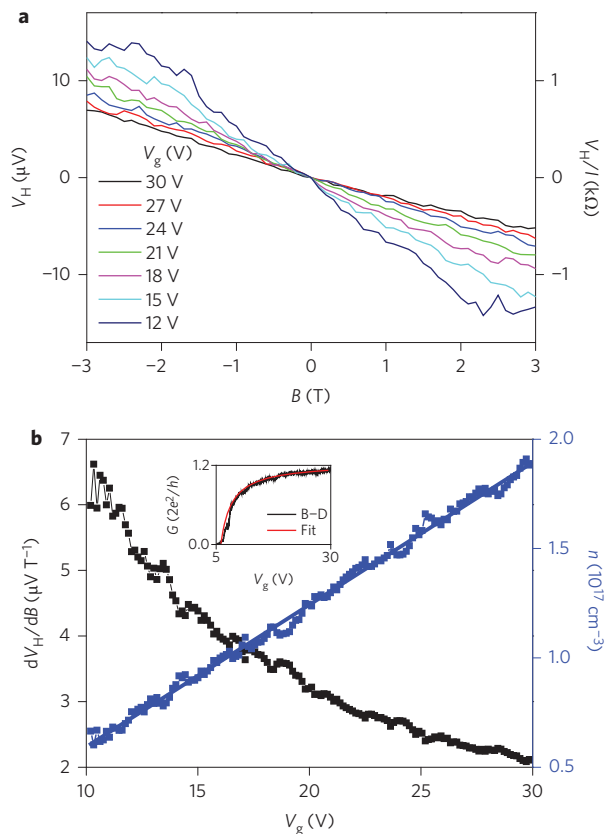
Figure 5 | Nanocross Hall measurements. a, Hall voltages, $V_H = V_B - V_D$, obtained by application of 10 nA a.c. current I through C–A with magnetic field B, at several gate voltages V_g. Measured traces have an offset of ~3 µV at $B = 0$ T, probably a longitudinal voltage, which has been subtracted. The trace at $V_g = 12$ V is an average of three traces. All other traces are obtained in a single measurement. Right axis: Hall resistance, V_H/I. **b**, From the Hall slope, dV_H/dB (left axis), the electron density n (right axis) as a function of gate voltage is extracted. A linear fit of $n(V_g)$ (blue line) gives $dn/dV_g = 6.5 \times 10^{15}$ cm^{-3} V^{-1}, and therefore capacitance $C = 51$ aF for channel B–D (Supplementary Section S3). This capacitance is used in a fit to gate trace B–D (see inset) and yields a mobility of 8,000 cm^2 V^{-1} s^{-1}.

Figure 6 | Gate-tunable supercurrent through a nanocross. Data taken at 20 mK. Instrumental resistance has been subtracted. **a**, Top-view SEM image of the device. To decrease the wire diameter, the nanocross was etched by HCl in the growth chamber directly after growth[30]. Scale bar, 0.5 µm. Contact spacings are 440 nm (section A–B), 620 nm (A–C and B–C), 1,300 nm (A–D and B–D) and 1,480 nm (C–D). Contact material is NbTiN/Al (50/70 nm). **b**, $V(I)$ characteristics for current bias I between contacts A–C (global backgate voltage $V_g = 14.8$ V, blue) and B–C ($V_g = 14.4$ V, black). The asymmetry in the $V(I)$ trace, indicating hysteresis, is due to environmental shunting[31] or self-heating of the device[32]. The kinks in the dissipative branches (indicated with asterisks) are probably Fiske steps[33,34]. Both features are commonly observed in underdamped Josephson junctions. In Supplementary Fig. S18 we show that these features also occur in our InSb nanowire Josephson junctions. Inset: $V(I)$ characteristic for section C–D ($V_g = 13.5$ V). **c**, Colour plot: differential resistance, dV/dI, as a function of I and V_g for section B–C. The black region ($dV/dI = 0$) indicates supercurrent through the nanocross. Superimposed with the same horizontal and vertical scale is the critical current for B–C (white), A–B (green) and A–C (blue).

projection. The histogram in Fig. 2e shows a maximum around $\Delta\varphi = 60°$. This maximum can be explained by the triangular cross-sectional shape of the InAs segment (Supplementary Fig. S3). During the annealing step, droplets fall to a lateral facet, leading to six preferential directions for $\Delta\varphi$ and a maximum around 60°. Owing to stem evaporation, it is also possible for small InAs diameters to change the cross-section from a triangle to a hexagon. In this particular case a droplet can cover more than one facet because of its large volume in comparison with the stem diameter, leading to smaller maxima every $\Delta\varphi = 30°$ (Fig. 2e, Supplementary Fig. S4).

During the final step of the process, the wires can merge and form a planar, branched nanowire structure, in this case either T- or X-shaped. The formation of a T or X structure depends on the level of alignment of two InSb nanowires in the vertical direction (Fig. 2f). When the wires are slightly misaligned in altitude, a cross is formed. During axial growth, the wire also grows in the radial direction. For InSb this radial growth mainly takes place just below the gold catalyst particle due to the catalytic decomposition of the trimethyl antimony (TMSb) precursor by the gold. The decomposed material can then either lead to axial or radial growth, soldering the two wires together. The vertical distance between two approaching wires can be reduced due to the flexibility

of the InAs stems, as shown in Fig. 2d. In that case, the InAs stem will bend during the merging process. For most crosses, the InAs stems are slightly bent, which is important for obtaining a high yield of crosses. More importantly, these flexible stems also allow small corrections of $\Delta\varphi$ in order to form single-crystalline crosses. This phenomenon, already observed for nanoparticles in solution[27], tends to align the crystalline orientations of both nanowires and can correct small misalignments (<2°). When the two wires are perfectly aligned in altitude, T shapes are formed. In this particular case, the droplet of one wire touches the second exactly in the middle of the nanowire. The catalyst particle will bounce and either move along one of the side facets or get stuck by wetting a re-entrant corner. As a consequence, a T-shaped structure or nanowing is formed (Supplementary Figs S7, S8).

The crystalline quality of these junctions was studied by high-resolution transmission electron microscopy (HR-TEM) for crosses with different joining angles. When the crossing angle between two InSb nanowires growing along a (111)B direction is $\Delta\varphi = 70.5°$ (Fig. 3a), the crystalline directions of both branches are aligned and a single-crystalline structure is formed. (Depending on the polarity orientation of the two wires, a twinned junction can also be obtained.) HR-TEM images of a single-crystalline cross, obtained just below the droplets of each

branch, are shown in Fig. 3b,c. The related fast Fourier transforms (FFTs) are presented in Fig. 3d,e. The perfect match of the FFT patterns proves that the cross in Fig. 3a is a single crystal, paving the way to advanced electronic transport devices. TEM data of junctions with different $\Delta\varphi$ angles are provided in Supplementary Figs S5, S6 and S7. In the most probable case ($\Delta\varphi = 60°$), the merging process occurs for two nanowires with different crystalline orientations only sharing horizontally oriented (110) planes at the same altitude. In this case, a Moiré fringe pattern characteristic of the interference of two different crystalline directions appears in the HR-TEM images. Interestingly, the crystalline orientation of each branch is the same before and after the junction, and the only defect in the structure is the grain boundary at the junction (Supplementary Figs S5, S6).

We next investigated the electrical transport properties through merged nanowires. A nanocross was contacted (Fig. 4a, inset) and the electron density controlled with a global backgate. The two-point resistance can be modulated by a gate potential between 7 and 15 kΩ and pinch-off for all contact pairs (Fig. 4a). The linear $I–V$ sweeps obtained for all contact combinations (Fig. 4b,c) indicate ohmic contacts and the absence of localization in the nanocross. This indicates that the interface at the intersection of the two wires is sufficiently transparent to allow transport from wire to wire without a tunnelling barrier.

To assess the carrier mobility in the nanocross, we extracted the electron density from Hall measurements. The standard method in electrical characterization of nanowires is the extraction of field-effect mobility from gate traces. However, this method has the drawback that it requires accurate knowledge of the capacitance between gate and nanowire, which is often lacking. Merged nanowires allow us to experimentally extract the nanowire capacitance from measurements of carrier density as a function of backgate voltage. It should be noted that approximations made to the nanocross device geometry and transport regime limit the accuracy of our mobility estimate (Supplementary Section S3).

Gate-tunable Hall resistances of ∼1 kΩ at $B \approx 3$ T were obtained (Fig. 5a). The electron density n, extracted from these Hall measurements, increases linearly with gate voltage (Fig. 5b), from ∼5×10^{16} cm^{-3} to ∼2×10^{17}cm^{-3}. Gate–nanocross capacitances of ∼50 aF were derived from a linear fit of $n(V_g)$. We then extracted the field-effect mobility from a fit to the gate traces of Fig. 4a (see inset of Fig. 5b for channel B–D) and found mobilities of ∼6,500–9,000 cm^2 V^{-1} s^{-1}. The same analysis for a second nanocross device (Supplementary Section S3) yielded mobilities of ∼6,700–10,000 cm^2 V^{-1} s^{-1}. These high mobilities reflect the high structural quality of our InSb nanocrosses. Moreover, these mobilities indicate that the favourable transport properties of InSb nanowires are preserved in complex wire structures. Nanocross sections with and without a grain boundary show similar mobility. Moreover, gate traces of nanocrosses and T junctions with various crossing angles $\Delta\varphi$ between 40° and 70° are comparable. Accordingly, the mobility is probably limited by factors other than the grain boundary, such as scattering at the surface or at impurities.

Because superconductivity is a key ingredient for the creation of Majorana fermions, it is essential to induce supercurrent in nanocrosses. Superconducting leads were therefore deposited at each end of a nanocross (Fig. 6a). The contact pairs of the device have a normal state conductance at large positive gate voltage between $1.1G_0$ and $3.5G_0$ ($G_0 = 2e^2/h$). The $V(I)$ characteristic of all measured contact pairs exhibits a supercurrent branch, indicating proximity-induced superconductivity[28,29]. Switching to a resistive state occurs when the current bias exceeds the critical current I_c (Fig. 6b). I_c is gate-tunable (Fig. 6c) and increases with the nanocross normal state conductance. By comparing different contact pairs, we find that I_c depends on the contact separation and varies between ∼4.6 nA (section A–C, separation of 620 nm) and

∼0.25 nA (C–D, separation of 1.5 μm). The critical currents within a single nanowire (section A–C) and through the nanocross junction (B–C) are comparable. Moreover, the supercurrents through these nanocross sections are similar to that through an InSb nanowire Josephson junction contacted with the same superconductor and with similar contact separation (Supplementary Fig. S18). These results substantiate the expectation that crossed nanowires will enable advances in topological superconducting systems such as the development of the proposed Majorana fermion braiding devices.

There are a few remaining challenges for these structures. The first is to increase the mobility to obtain ballistic transport between all contacts. The mobility may be enhanced by passivating the wire with a shell of wide-bandgap material. InSb has a large lattice constant and most ternary AlInSb or InGaSb compounds would be suitable as a shell material. The second challenge is to improve the yield of single-crystalline crossed wires. With the current approach, ∼8% of the nanocrosses have an optimal merging angle. One option to improve this is the use of (001)-oriented substrates[23]. Wires growing along two ⟨111⟩B directions will meet, and if their epitaxial relation with the substrate is maintained, they will form a single-crystalline structure.

References

1. Majorana, E. A symmetric theory of electrons and positions. *Soryushiron Kenkyu* (Engl. Transl.) **63,** 149 (1981) [translation from Teoria simmetrica dell'electtone e del positrone. *Nuovo Cimento* **14,** 171 (1937)].
2. Mourik, V. *et al.* Signatures of Majorana fermions in hybrid superconductor–semiconductor nanowire devices. *Science* **336,** 1003–1007 (2012).
3. Das, A. *et al.* Zero-bias peaks and splitting in an Al–InAs nanowire topological superconductor as a signature of Majorana fermions. *Nature Phys.* **8,** 887–895 (2012).
4. Deng, M. T. *et al.* Anomalous zero-bias conductance peak in a Nb–InSb nanowire–Nb hybrid device. *Nano Lett.* **12,** 6414–6419 (2012).
5. Freedman, M. H., Kitaev, A., Larsen, M. J. & Wang, Z. Topological quantum computation. *Bull. Am. Math. Soc.* **40,** 31–38 (2003).
6. Nayak, C., Simon, S. H., Stern, A., Freedman, M. & Das Sarma, S. Non-Abelian anyons and topological quantum computation. *Rev. Mod. Phys.* **80,** 1083–1159 (2008).
7. Kitaev, A. Fault-tolerant quantum computation by anyons. *Ann. Phys.* **303,** 2–30 (2003).
8. Wilczek, F. Majorana returns. *Nature Phys.* **5,** 614–618 (2009).
9. Lutchyn, R. M., Sau, J. D. & Das Sarma, S. Majorana fermions and a topological phase transition in semiconductor–superconductor heterostructures. *Phys. Rev. Lett.* **105,** 077001 (2010).
10. Oreg, Y., Refael, G. & von Oppen, F. Helical liquids and Majorana bound states in quantum wires. *Phys. Rev. Lett.* **105,** 177002 (2010).
11. Alicea, J., Oreg, Y., Refael, G., von Oppen, F. & Fisher, M. P. A. Non-abelian statistics and topological quantum information processing in 1D wire networks. *Nature Phys.* **7,** 412–417 (2011).
12. van Heck, B., Akhmerov, A. R., Hassler, F., Burrello, M. & Beenakker, C. W. J. Coulomb-assisted braiding of Majorana fermions in a Josephson junction array. *New J. Phys.* **14,** 035019 (2012).
13. Hyart, T. *et al.* Flux-controlled quantum computation with Majorana fermions. *Phys. Rev. B* **88,** 035121 (2013).
14. Algra, R. E. *et al.* Twinning superlattices in indium phosphide nanowires. *Nature* **456,** 369–372 (2008).
15. Wen, C-Y. *et al.* Periodically changing morphology of the growth interface in Si, Ge, and GaP Nanowires. *Phys. Rev. Lett.* **107,** 025503 (2011).
16. Glas, F., Harmand, J-C. & Patriarche, G. Why does wurtzite form in nanowires of III–V zinc blende semiconductors? *Phys. Rev. Lett.* **99,** 146101 (2007).
17. Dick, K. A. *et al.* Synthesis of branched 'nanotrees' by controlled seeding of multiple branching events. *Nature Mater.* **3,** 380–384 (2004).
18. Yun, S. H., Wu, J. Z. Dibos, A., Zou, X. & Karlsson, U. O. Self-assembled boron nanowire Y-junctions. *Nano Lett.* **6,** 385–389 (2006).
19. Jiang, X. *et al.* Rational growth of branched nanowire heterostructures with synthetically encoded properties and function. *Proc. Natl Acad. Sci. USA* **108,** 12212–12216 (2011).
20. Manna, L., Milliron, D. J., Meisel, A., Scher, E. C. & Alivisatos, A. P. Controlled growth of tetrapod-branched inorganic nanocrystals. *Nature Mater.* **2,** 382–385 (2003).

863

21. Dai, X. *et al*. Tailoring the vapor–liquid–solid growth toward the self-assembly of GaAs nanowire junctions. *Nano Lett.* **11**, 4947–4952 (2011).
22. Suyatin, D. B. *et al*. Electrical properties of self-assembled branched InAs nanowire junctions. *Nano Lett.* **8**, 1100–1104 (2008).
23. Dalacu, D., Kam, A., Austing, D. G. & Poole, P. J. Droplet dynamics in controlled InAs nanowire interconnections. *Nano Lett.* **13**, 2676–2681 (2013).
24. Wagner, R. S. & Ellis, W. C. Vapor–liquid–solid mechanism of single crystal growth. *Appl. Phys. Lett.* **4**, 89–90 (1964).
25. Plissard, S. R. *et al*. From InSb nanowires to nanocubes: looking for the sweet spot. *Nano Lett.* **12**, 1794–1798 (2012).
26. Van Weperen, I. *et al*. Quantized conductance in an InSb nanowire. *Nano Lett.* **13**, 387–391 (2013).
27. Li, D. *et al*. Direction-specific interactions control crystal growth by oriented attachment. *Science* **336**, 1014–1018 (2012).
28. Doh, Y-J. *et al*. Tunable supercurrent through semiconductor nanowires. *Science* **309**, 272–275 (2005).
29. Xiang, J. *et al*. Ge/Si nanowire mesoscopic Josephson junctions. *Nature Nanotech.* **1**, 208–213 (2006).
30. Borgström, M. T. *et al*. *In situ* etching for total control over axial and radial nanowire growth. *Nano Res.* **3**, 264–270 (2010).
31. Kautz, R. L. & Martinis, J. M. Noise affected *I–V* curves in small hysteretic Josephson junctions. *Phys. Rev. B* **42**, 9903–9937 (1990).
32. Courtois, H. *et al*. Origin of hysteresis in a proximity Josephson junction. *Phys. Rev. Lett.* **101**, 067002 (2008).
33. Fiske, M. D. Temperature and magnetic field dependences of Josephson tunneling current. *Rev. Mod. Phys.* **36**, 221–222 (1964).
34. Coon, D. D. & Fiske, M. D. Josephson AC and step structure in supercurrent tunneling characteristic. *Phys. Rev.* **138**, A744–A746 (1965).

Author contributions

S.R.P. and E.P.A.M.B. supervised the experiments. G.W.G.I., S.R.P., D.C. and E.P.A.M.B. grew the T- and X-shaped nanowires. S.R.P. performed the XRD measurements. M.V. analysed the structures using TEM. I.v.W., J.K., L.J.C. and D.B.S. fabricated the cross devices and performed the electrical measurements. I.v.W., J.K., L.J.C., D.B.S., A.G., S.M.F. and L.P.K analysed the electrical data. The manuscript was prepared with contributions from all authors.

Additional information

Supplementary information is available in the online version of the paper. Reprints and permissions information is available online at www.nature.com/reprints. Correspondence and requests for materials should be addressed to S.R.P. and E.P.A.M.B.

Competing financial interests

The authors declare no competing financial interests.